



# Lab on a Chip

## Metasurface-enhanced Infrared Spectroscopy in multiwell format for real-time assaying of live cells

Journal:	<i>Lab on a Chip</i>
Manuscript ID	LC-ART-01-2023-000017.R1
Article Type:	Paper
Date Submitted by the Author:	16-Mar-2023
Complete List of Authors:	Huang, Steven; Cornell University, Applied and Engineering Physics Sartorello, Giovanni; Cornell University, Applied and Engineering Physics Shen, Po-Ting; Cornell University, Applied and Engineering Physics Xu, Chengqi; Weill Cornell Medicine, Caryl and Israel Englander Institute for Precision Medicine; Cornell University, Meinig School of Biomedical Engineering Elemento, Olivier; Weill Cornell Medicine, Caryl and Israel Englander Institute for Precision Medicine Shvets, Gennady; Cornell University School of Applied and Engineering Physics, School of Applied and Engineering Physics

SCHOLARONE™  
Manuscripts

## ARTICLE

## Metasurface-enhanced Infrared Spectroscopy in multiwell format for real-time assaying of live cells

Received 00th January 20xx,  
Accepted 00th January 20xx

Steven H. Huang<sup>\*a</sup>, Giovanni Sartorello<sup>a</sup>, Po-Ting Shen<sup>a</sup>, Chengqi Xu<sup>b,c</sup>, Olivier Elemento<sup>\*b</sup>, and Gennady Shvets<sup>\*a</sup>

DOI: 10.1039/x0xx00000x

Fourier transform infrared (FTIR) spectroscopy is a popular technique for the analysis of biological samples, yet its application in characterizing live cells is limited due to the strong attenuation of mid-IR light in water. Special thin flow cells or attenuated total reflection (ATR)-FTIR have been used to mitigate this problem, but these techniques are difficult to integrate into standard cell culture workflow. In this work, we demonstrate that the use of plasmonic metasurface fabricated on planar substrates and the probing of cellular IR spectra through metasurface-enhanced infrared spectroscopy (MEIRS) can be an effective technique to characterize the IR spectra of live cells in a high-throughput manner. Cells are cultured on metasurfaces integrated with multiwell cell culture chambers and are probed from the bottom using an inverted FTIR microspectrometer. To demonstrate the use of MEIRS as a cellular assay, cellular adhesion on metasurface with different surface coatings as well as cellular response to the activation of protease-activated receptor (PAR) signaling pathway were characterized through the changes in cellular IR spectra.

### Introduction

Infrared (IR) spectroscopy is a label-free, non-destructive analytical method with chemical specificity provided by molecular vibrations. Traditionally limited to Fourier transform infrared (FTIR) spectroscopy but recently also expanded to include quantum cascade laser (QCL) based wavelength-scanning spectroscopy, IR spectroscopy has seen expanding areas of applications in biology and life sciences.<sup>1,2</sup> These include, to name just a few, the analysis of protein samples for research or quality control,<sup>3–5</sup> the analysis of bio-fluid samples such as blood serum and plasma for disease screening,<sup>6–8</sup> the spectro-chemical imaging of histology samples as “digital staining”,<sup>9–12</sup> as well as the spectroscopy and spectro-chemical imaging of fixed cells, live cells, or cell lysate to study cell biology.<sup>13–17</sup> IR spectroscopy-based monitoring of live cells in real time is particularly appealing because it enables quantitative measurements of dynamic cellular changes, such as growth, metabolism, differentiation, and cell-drug interaction, without missing any key biological events. In addition, avoiding cell fixation and drying simplifies the experiment by making the sample preparation less labor-intensive and avoiding possible experimental artifacts.

Despite these advantages of live cell measurement, most IR spectroscopy studies of cells still use dried and fixed samples because live cell measurement is challenging due to the strong attenuation of mid-IR light in water. Measuring the IR spectra of live cells in culture medium or buffer solution is possible, but this requires the optical path length of the mid-IR light in water to be limited to 10  $\mu\text{m}$  or smaller,<sup>18</sup> and thus requiring the use of customized setups designed for this purpose. There are mainly two approaches to limit the optical path length. The first is to measure the IR spectra in transmission or transfection mode, with cells maintained in thin microfluidic devices or liquid compartments sandwiched by two IR transparent windows.<sup>13,17,19–21</sup> Such devices have been especially successful in the studies that use synchrotron radiation FTIR spectroscopy and spectro-chemical imaging, where the high brightness of synchrotron source further mitigates the issues caused by water absorption.<sup>17,22–24</sup> The second approach is to use attenuated total reflection (ATR)-FTIR, in which cells are grown on either a single-bounce or multi-bounce ATR crystal, and the evanescent field from total internal reflection of mid-IR light at the crystal/cell interface is used to probe the IR spectrum of the cells.<sup>15,16,18,25,26</sup> In the ATR-FTIR approach, the effective penetration of the evanescent field into the cell and surrounding culture medium is roughly 1–2  $\mu\text{m}$ , and the absorption spectra are not impeded by water absorption. Both spectro-chemical imaging of live cells, as well as time course measurements to observe cellular metabolism and cell-drug interactions, have been demonstrated using ATR-FTIR.

The key to high-throughput measurements is the microplate format, which allows for the manipulation and testing of many samples in parallel. Cellular assays in microplate format based on absorbance and fluorescence are already widely in use for

<sup>a</sup> School of Applied and Engineering Physics, Cornell University, Ithaca, New York, USA 14853

<sup>b</sup> Caryl and Israel Englander Institute for Precision Medicine, Weill Cornell Medicine, New York, NY, 10021.

<sup>c</sup> Meinig School of Biomedical Engineering, Cornell University, Ithaca, NY, 14853

\*Email: hh623@cornell.edu, ole2001@med.cornell.edu, gshvets@cornell.edu

Electronic Supplementary Information (ESI) available: [details of any supplementary information available should be included here]. See DOI: 10.1039/x0xx00000x

many life science applications. Live cell assays in microplate format have also been integrated with label-free phenotypical cellular assays, such as cellular impedance biosensors based on microelectrodes and optical biosensors based on resonant waveguide gratings (RWGs) and photonic crystals.<sup>27–34</sup> These devices were applied to the measurements of cell adhesion, cellular signaling, cellular response to chemotherapeutics, as well as drug screening applications. Ideally, FTIR measurements of live cells can be made in microplate format as well. Live cell FTIR spectroscopy in microplate format would be easily integrated into standard cell culture workflow, suitable for long-term cell culture and observation, and compatible with many existing instruments such as absorbance and fluorescence plate readers. Unfortunately, neither of the two live cell FTIR approaches are compatible with the microplate format in their current forms. Thin perfusion cells, while capable of continuously providing the cells with fresh culture and maintaining their vitality for multiple days, are incompatible with open-top independently-accessible multi-well structures. Likewise, although ATR-FTIR-based spectroscopic imaging has been demonstrated as a useful tool for the high-throughput measurement of microarrays of liquid samples,<sup>35,36</sup> the small size and non-planar geometry of a single-bounce internal reflection element limits the available sensing area and make it difficult to scale-up this technique for larger, microplate-based cellular assays. Larger and planar multi-bounce internal reflection elements are available, but the requirement for a specific incidence angle and the multiple reflections of IR beam within the internal reflection element make it difficult to probe each well independently.<sup>15,16</sup>

Recently, our group has developed metasurface-enhanced infrared spectroscopy (MEIRS) and applied it to measuring the IR spectra of live cells.<sup>37</sup> In MEIRS, cells are grown on periodic arrays of engineered plasmonic nanoantennas (*i.e.* metasurfaces) and the IR spectra of the cells are obtained from the reflectance spectrum of the metasurface, through surfaced-enhanced IR absorption (SEIRA). In SEIRA, IR absorption of analyte in proximity to resonant nanoantennas are enhanced by several orders of magnitude through localized hotspots of electromagnetic field. IR spectroscopy through nanoantenna and metasurface based SEIRA has been extensively studied and applied to the spectroscopic measurement of self-assembled monolayers as well as biomolecules such as protein monolayers, lipid bilayers, and lipid vesicles.<sup>38–43</sup> Applied to the IR spectroscopy of cells, the localized field enhancement and evanescent field penetration (on the order of 100 nm) make MEIRS only sensitive to cellular changes in a shallow detection zone. MEIRS shares some similarities with ATR-FTIR in that the optical measurement is carried out in reflection, thus avoiding the passing mid-IR light through a thick layer of water. Consequently, MEIRS is insensitive to the depth of the water layer covering the cells. Cellular events that can be detected in real-time using MEIRS include changes in the cellular membrane (*e.g.*, redistribution of cellular matter around it), as well as changes in cell adhesion and cytoskeletal reorganization. By integrating MEIRS with a closed microfluidic perfusion-based system, we have monitored cellular responses to trypsinization

and cholesterol depletion, as well as cell-drug interactions with chemotherapeutics.<sup>37,44</sup> Chemical imaging of adherent cells with single-cell resolution has also been demonstrated using MEIRS,<sup>37</sup> albeit at the expense of time resolution.

In its microfluidic implementation,<sup>37,44</sup> MEIRS is carried out using an upright IR microscope while the cells are located near the top of the perfusion chamber (*i.e.* in the “upside-down” position). As a result, a microfluidics-based MEIRS has several geometry-related drawbacks that could be potentially resolved by using an inverted IR microscope. First, the bulky perfusion setup makes it difficult to move the sample, and the cells cannot be easily moved in and out of the incubator. Second, the location of a cell-covered metasurface at the top of chamber excludes integration with open micro-well structures. Third, occasional formation of air bubbles inside the perfusion chamber, and their subsequent rise to the top of the chamber, disrupts the measurement and the cells, making long-term measurement difficult.

In this work, we report the integration of a metasurface with a multi-well cell culture chamber to form a device allowing for MEIRS measurement in the Multiwell-Integrated Metasurface Array (MIMA) format. An inverted IR micro-spectrometer setup is constructed as an add-on to FTIR spectrometer to probe this device. IR spectra are measured in reflection mode through an IR-transparent CaF<sub>2</sub> substrate (Fig. 1(a)). A previously designed bi-resonant plasmonic metasurface is used for this work (Fig. 1(b)), with cells cultured directly on top of the metasurface (Fig. 1(c)). Each meta-atom in the array supports two resonances, a Lorentzian dipolar resonance at  $\omega_D = 2900 \text{ cm}^{-1}$  and a quadrupolar resonance at  $\omega_Q = 2080 \text{ cm}^{-1}$ , which has a Fano-like lineshape due to its interaction with the dipolar resonance. When this metasurface is used to measure the IR absorption of molecules, the molecular vibrational bands appear overlapped on top of a broad plasmonic resonance, due to the interaction between the two (Fig. 1(d), upper panel). Further, the plasmonic resonance may shift depending on the local refractive index. Such resonance shift is present across the entire spectrum, but is most prominent around  $\omega_Q$ . More detailed descriptions of the optical resonance supported by this plasmonic metasurface had been published elsewhere.<sup>37,41,45,46</sup> The cellular absorbance spectra are obtained from the measured reflectance spectra as  $A(\omega) = -\log_{10}(R^{(\text{cell})}(\omega)/R^{(\text{bare})}(\omega))$ , where  $R^{(\text{cell})}(\omega)$  and  $R^{(\text{bare})}(\omega)$  are the reflectance spectra from metasurface with and without cells, respectively. The absorbance and second derivative absorbance spectra (Fig. 1(d), middle and lower panel) are then analyzed using principal component analysis (PCA) to extract the temporal changes in the IR spectra, with particular focus on the three spectral windows corresponding to protein and lipid-related IR absorption (shaded red and gray), as well as the frequency shift of the plasmonic resonance of the metasurface (shaded yellow) caused by overall refractive index changes of the metasurface surrounding. Two proof-of-concept spectroscopic measurements are presented: (i) cell adhesion and spreading on substrates with different surface coatings, and (ii) cellular response to the activation of protease-activated receptor (PAR) pathway by synthetic peptides.

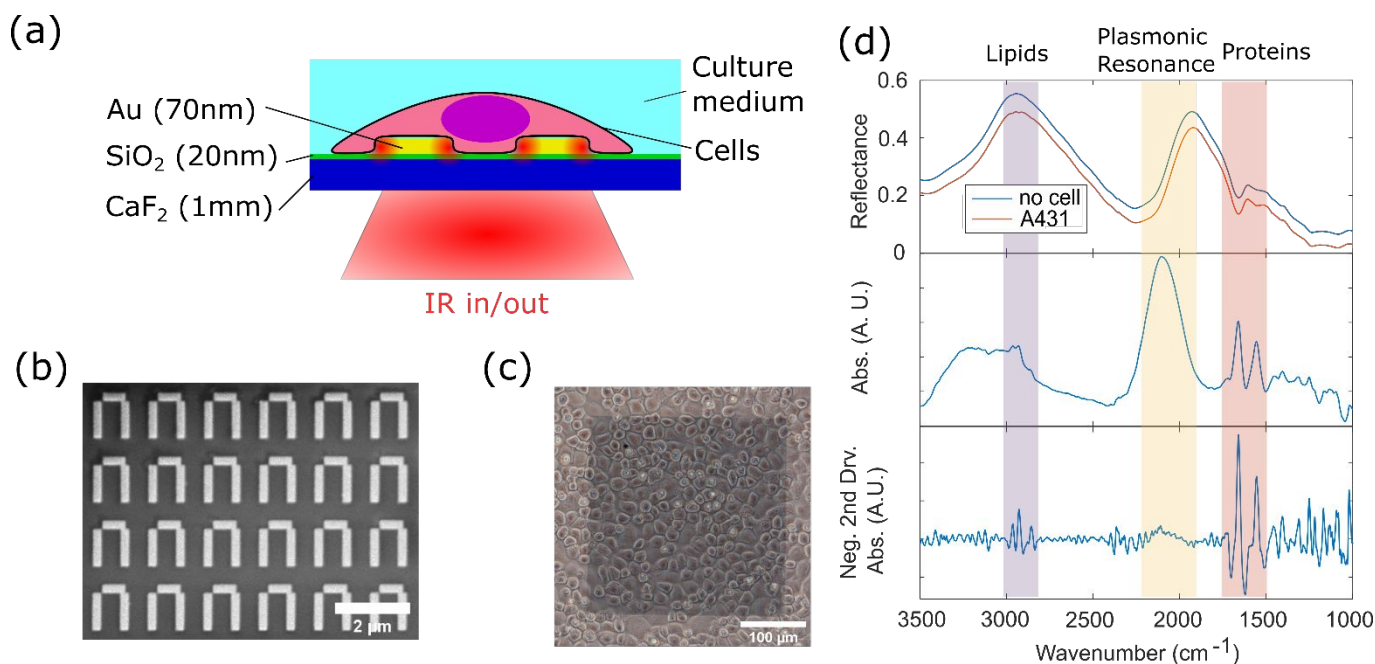


**Figure 1.** (a) Schematic drawing of the MEIRS measurement. (b) Scanning electron microscope (SEM) image of the nanoantenna array comprising the metasurface. Scale bar: 2  $\mu\text{m}$ . (c) Phase contrast image of A431 cells cultured on the metasurface. Scale bar: 100  $\mu\text{m}$ . (d) Representative IR spectra: reflectance (top) from a metasurface without (blue) and with (red) cells, offset by 5% for clarity. Absorbance spectrum (middle) and its negative 2<sup>nd</sup> derivative (bottom) attributed to the cells. The absorbance spectra are obtained from the difference between bare and cell-covered metasurfaces.

## Results and Discussions

### Fabrication of Multiwell Integrated Metasurface Array (MIMA)

Plasmonic metasurface were fabricated on a 1"  $\times$  3"  $\times$  1 mm thick slide of  $\text{CaF}_2$  and integrated with superstructure for multiwell cell culture chamber. First, metasurface patterns were fabricated on a 4" diameter circular  $\text{CaF}_2$  window as described in detail elsewhere<sup>37,41,45,46</sup> and in the Experimental Section. As the final step, the 4" diameter circular  $\text{CaF}_2$  window was diced into two 1"  $\times$  3" slides. Each slide contains 16 identical patterns, each of which includes one 300  $\mu\text{m}$   $\times$  300  $\mu\text{m}$  gold square (for background measurement) as well as four 300  $\mu\text{m}$   $\times$  300  $\mu\text{m}$  arrays of metasurface patterns: see Fig. 2(a). These 16 patterns follow standard 96 well plate spacing and match the well spacing of the multiwell superstructure. We used CS16-CultureWell™ Removable Chambered Coverglass (Grace Bio-Labs) as the multiwell superstructure. This cell culture chamber uses silicone well gaskets to form a leak-proof seal between the multiwell superstructure and a glass coverslip. For our device, the original glass coverslip was substituted by the  $\text{CaF}_2$  slide with the metasurface array fabricated on it. The attachment of the slide using silicone gaskets enables the removal of the former if needed, for example, to clean the metasurface or to take SEM images. Photographs of the assembled MIMA are presented in Figs. 2 (b)-(d). Our current prototype MIMA structure is smaller than a standard microplate, but the fabrication can be scaled up for larger structures with more wells.

### Optical Setup

Currently, commercially available FTIR-coupled IR microscopes are only available in upright configuration. This is to be

expected: inverted microscopes are typically intended for live cell measurement in culture dishes and microplates, but such measurement is not possible in the mid-IR band due to the absorption of light passing through a water-filled microwell. However, an inverted IR microscope is exactly what is needed for a MIMA device that enables reflection-based live cell measurements in an aqueous environment. To accommodate this, an in-house optical setup was assembled as an add-on to an existing FTIR spectrometer. Fig. 3 presents the schematic drawing of our inverted IR micro-spectroscopy setup. Thermal light source from Bruker Vertex 70 FTIR spectrometer is coupled out from an external port and focused onto the metasurface from the bottom using a 15X reflective Cassegrain objective. The objective is adjusted in the vertical direction through a manual zoom housing for focusing. The reflected beam from the metasurface is directed towards a liquid  $\text{N}_2$  cooled mercury-cadmium-telluride (MCT) detector using a ZnSe beam splitter. Additionally, a visible white-light epi-illumination and imaging system, which uses the same reflective Cassegrain objective, is used for locating the metasurface and identifying the areas of interest. For sequential interrogation of different metasurface array elements located at the bottoms of their respective microwells, the MIMA device is mounted on a XY microscope linear translation stage.

### IR spectroscopic measurement of cellular adhesion to metasurface with different surface coatings

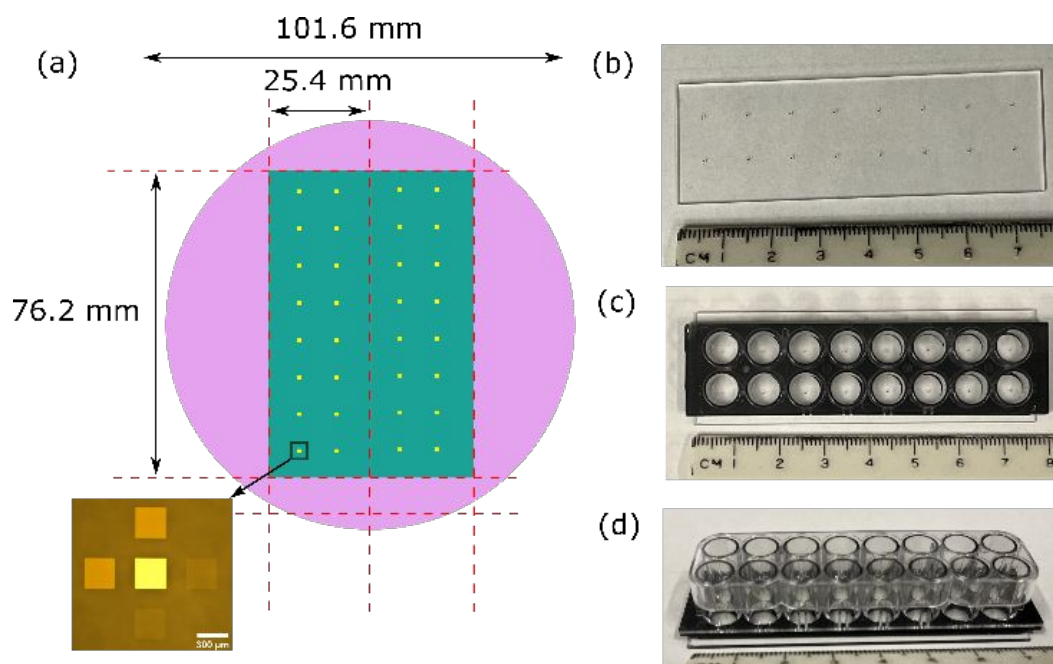


**Figure 2.** Multiwell Integrated Metasurface Array (MIMA) device. (a) Schematic drawing of a metasurface array fabricated on a 4" diameter  $\text{CaF}_2$  window. Red dotted lines: cuts made by dicing saw. Inset: a single metasurface array element comprising one gold reference pixel and four metasurface pixels for each well. Scale bar: 300  $\mu\text{m}$ . (b) 16 metasurface array elements after dicing the  $\text{CaF}_2$  window into two 1" x 3" slide. (c) Top and (d) side views of MIMA.

As the first proof-of-concept demonstration, we have used the MIMA device to spectroscopically characterize cell adhesion to metasurfaces coated with different surface coatings. An adherent cell line A431 (human epidermoid carcinoma) was used for these experiments. Cell adhesion is of fundamental importance to cell-surface interactions. Different surface coatings are routinely used for culturing cells on flat substrates, including collagen, laminin, fibronectin, poly-D-lysine (PDL).<sup>32-34,47,48</sup> The effectiveness of these surface coatings for different cell lines can be difficult to predict *a priori*, and typically needs to be determined experimentally. We use a 16-well MIMA to interrogate cells adhesion to four different coating conditions: no coating, fibronectin, poly-D-lysine, as well as 10% fetal bovine serum, which simulates typical cell culture conditions.

A431 cells were trypsinized from culture flask and suspended in serum-free Leibovitz's L15 medium designed to maintain physiological pH at ambient atmospheric conditions. Cells were seeded onto the 16-well MIMA just prior to measurement, and all FTIR-based measurements were performed at room temperature at 1 acquisition per minute. All wells were sequentially measured by moving the sample mounted on an XY translation stage, and then returning to the first well to repeat the cycle: see Fig. S1(a) for the stage movement pattern. Thus, one reflection spectrum  $R(\omega, t)$  was collected from each well every 16 minutes. Spectra acquisition was continued for about 6 hours, limited by the liquid  $\text{N}_2$  hold time of the MCT detector. Another set of measurements were taken 24 hours after initial seeding of the cells to collect the spectra of fully adhered and spread cells.

To analyze the collected spectra, we focused on three spectral windows: proteins absorption (1499  $\text{cm}^{-1}$  – 1807  $\text{cm}^{-1}$ ) attributed to amide I and amide II bands, lipids absorption (2756  $\text{cm}^{-1}$  – 3064  $\text{cm}^{-1}$ ) attributed to  $\text{CH}_2$  and  $\text{CH}_3$  stretchings, as well

as shift in plasmonic resonance (1845  $\text{cm}^{-1}$  – 2231  $\text{cm}^{-1}$ ) attributed to local refractive index changes. Time-dependent absorbance spectra  $A(\omega, t)$  defined as  $A(\omega, t) = -\log_{10}(R^{(\text{cell})}(\omega, t)/R^{(\text{bare})}(\omega))$ , where  $R^{(\text{cell})}(\omega, t)$  and  $R^{(\text{bare})}(\omega)$  are the reflectance spectra from metasurface with and without cells, respectively, provides a more intuitive representation of the cellular vibrational spectra on the metasurface. This is visualized in Fig. 1(d), where typical reflectance and absorbance spectra are plotted for fully adhered cells. The absorbance spectrum enables us to define the three abovementioned spectral regions, where the most pronounced spectral features can be observed. We specifically note that the plasmonic resonance shift peak at around 2100  $\text{cm}^{-1}$  is quite broad. The resonance shift affects all wavenumbers to varying degrees, and partially overlaps with the proteins and lipids absorption bands. Therefore, to better separate its contribution from those of proteins- and lipids-linked vibrations, second derivative absorption spectra  $\partial^2 A(\omega, t)/\partial \omega^2$  are used for the analysis of proteins and lipids absorption windows. Undifferentiated (*i.e.* 0<sup>th</sup> derivative) absorption spectra are used for the analysis of the plasmonic resonance shift.

For each spectral window, principal component analysis (PCA) was applied to the absorbance difference spectra defined as  $\Delta A \equiv A(\omega, t) - A(\omega, t = 0)$ . This was done to emphasize the spectral changes resulting from cellular adhesion, and to exclude the spectral contribution from different surface coatings. The first principal component (PC1) loadings plotted in Figs. 4 (a), (c), (e) represent the dominant modes of cell-related spectral change in each spectral window. The time dependent PC1 scores (see Figs. 4 (b), (d), (f) for each of the three spectral windows), which we refer to as cellular "signal", represent the temporal change of such spectral features. We

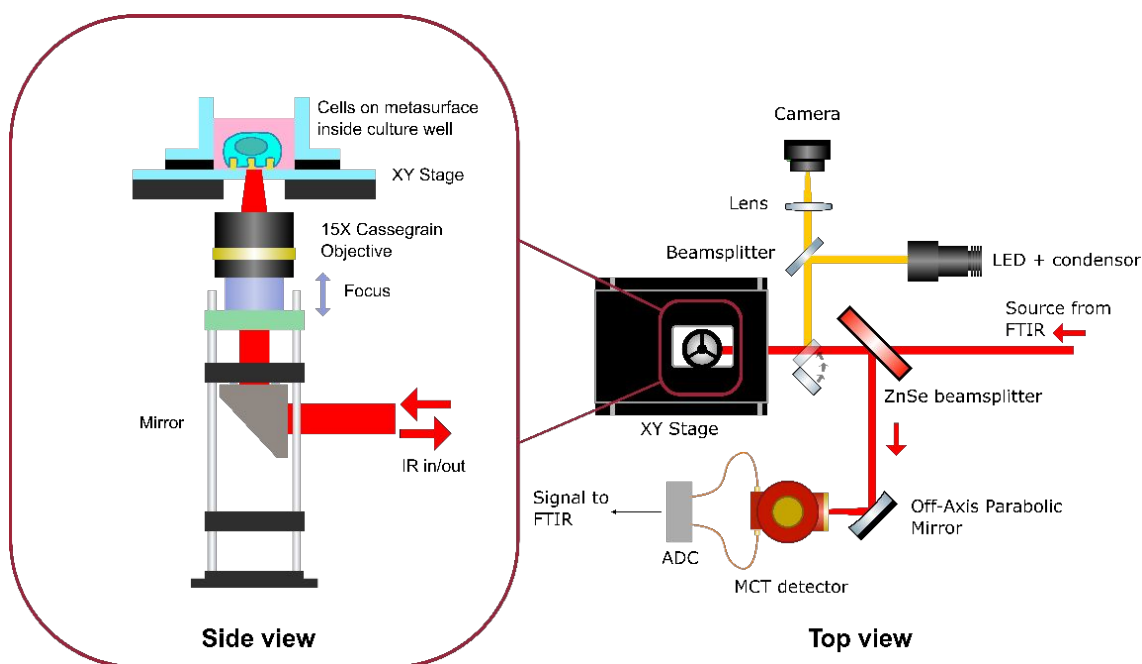


**Figure 3.** Schematic drawing of the inverted micro-spectroscopy setup. Red beam: broadband mid-IR light from thermal source used for IR spectroscopy. Yellow beam: visible white light used for locating and positioning the metasurface array elements at the bottoms of the wells.

only focused on PC1 in each spectral window for the ease of interpretation. While additional information is likely contained in the higher principal components, their temporal signals were not easily amenable to qualitative interpretation.

When the cells are seeded on a flat substrate, they first form attachment sites and anchor themselves to the substrate, then flatten and spread out,<sup>29</sup> thus increasing the overlap of cellular materials with the evanescent near-fields of the plasmonic metasurface. Such behaviour is reflected in the cellular signal from MEIRS measurement, as we see a gradual increase in proteins and lipids absorption, as well as a redshift in plasmonic resonance, as seen in the increase in plasmonic resonance signal. The spectral features that we observed for cellular adhesion through MEIRS (Figs. 4 (a), (c), (e)) were similar to those from typical FTIR measurement of cells or thin tissues in transmission mode or ATR-FTIR.<sup>1,2,12,13,16,20</sup> In the protein window, the spectral signature is dominated by amide I (centered at  $1656\text{ cm}^{-1}$ ) and amide II (centered at  $1552\text{ cm}^{-1}$ ) peaks. Additionally, a smaller peak at  $1741\text{ cm}^{-1}$  attributed to C=O stretching of the lipids can be observed. In the lipids window, the main spectral features include  $\text{CH}_2$  symmetric stretching at  $2856\text{ cm}^{-1}$ ,  $\text{CH}_2$  asymmetric stretching at  $2928\text{ cm}^{-1}$ , and  $\text{CH}_3$  asymmetric stretching at  $2966\text{ cm}^{-1}$ . A weaker peak that may be attributed to  $\text{CH}_3$  symmetric stretching is also observed at  $2881\text{ cm}^{-1}$ . In the plasmonic resonance window, no vibrational peaks are observed. Instead, a broad peak centered at  $2100\text{ cm}^{-1}$  is observed in the absorbance spectra due to the redshift of the plasmonic resonance. The redshift is caused by the refractive index of cellular matter being higher than that of water, which is displaced from the metasurfaces by attaching cells.

The temporal cellular signal in each spectral window (Figs. 4 (b), (d), (f)) clearly shows that cells respond differently to different surface coatings. Although we observed an increase in

cellular signal from cellular adhesion and spreading from all coatings, the amplitude and dynamics of the cellular signals were different. In the long term (after 24 hours), fibronectin coated metasurfaces resulted in the strongest cellular signal, followed by FBS coated, uncoated, and PDL coated metasurfaces. This is also reflected in cell morphology: phase contrast images clearly show that whereas cells spread well for fibronectin and FBS coated metasurfaces, cell spreading is limited for uncoated and PDL coated metasurfaces (Fig. S2). Our result is consistent with previous studies on cellular adhesion on different coating materials using electric impedance measurement, which found that fibronectin is often the best coating material among others, including collagen and PDL.<sup>32–34</sup> However, these studies had also found that the best coating material is often dependent on cell type and cell density, outlining the importance of testing different coating materials for specific experimental conditions.

The dynamics of cellular signal (Figs. 4 (b), (d), (f)) within 1 hour after seeding is markedly different from that after 24 hours; fibronectin coated metasurfaces still have the largest rate of increase in cellular signal, but PDL coated metasurfaces follows in the second, followed by uncoated metasurfaces in the third, and FBS coated metasurfaces in the last place. This observation of cellular adhesion dynamics suggests that there are two phases of cellular adhesion, likely corresponding to the initial anchoring of the cells on the metasurface and the spreading of cells that follows it. We note that cells were seeded at high density (approximately 100,000 cells per well) so that the initially seeded cells were enough to form a confluent monolayer on the metasurface, and hence the proliferation of cells likely did not play a significant role in the observed cellular signal. Interestingly, PDL coating resulted in rapid short-term increase in cellular signal within the first hour. This is consistent with well-established observations of rapid

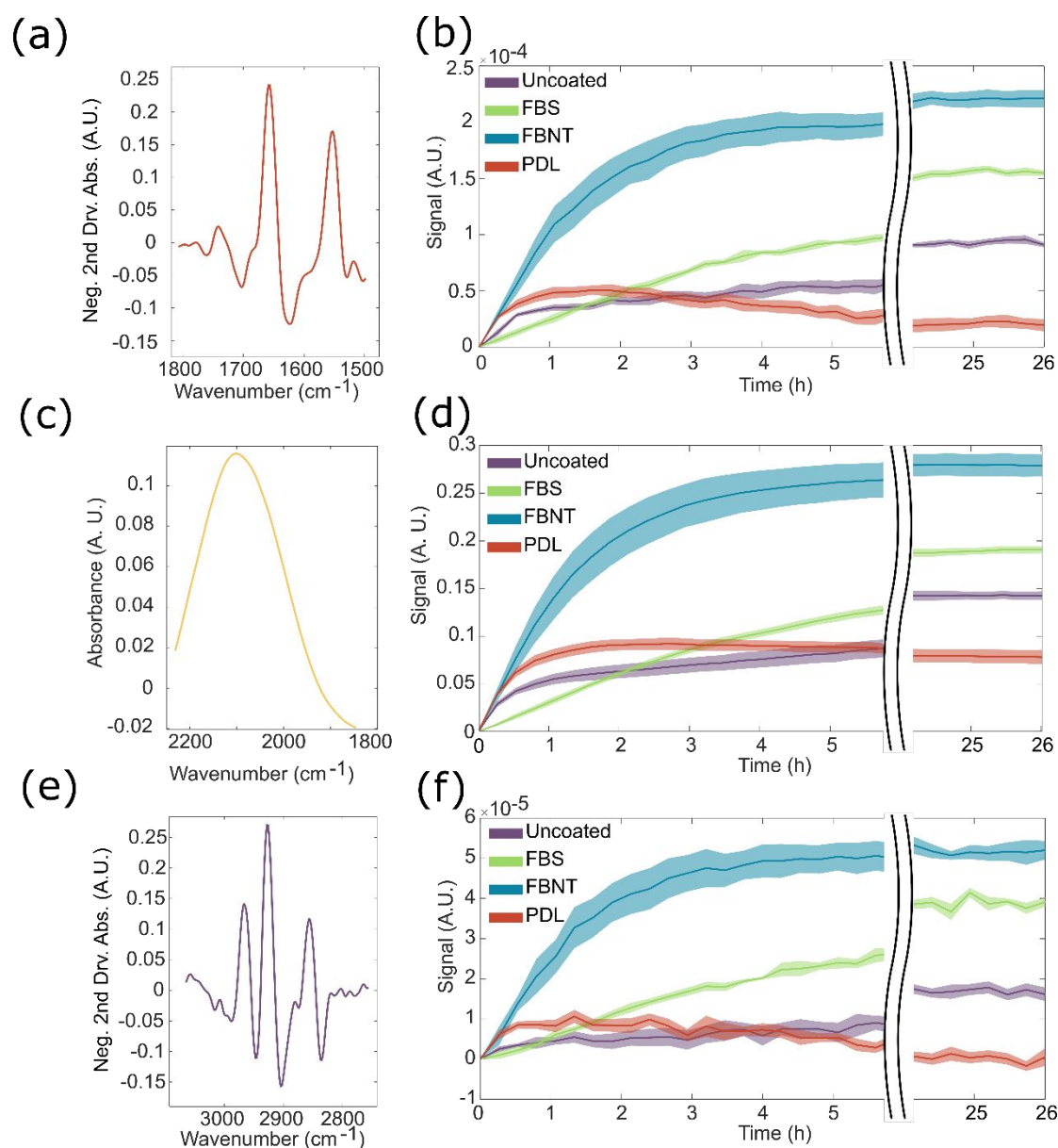


**Figure 4.** MEIRS measurement of A431 cell adhesion on metasurfaces with different surface coating. (a), (c), (e) PC1 loading in the protein (a), plasmonic resonance (b), and lipid (c) spectral windows. The signs of the 2<sup>nd</sup> derivative absorbance spectra for proteins and lipids have been reversed for more intuitive presentation. (b), (d), (f) Temporal cellular signal, obtained from PC1 score, in the protein, plasmonic resonance, and lipid spectral windows, respectively. Solid curves: mean signals. Shaded areas: the standard error ( $n = 4$ ). The data was taken for a 6-hour period immediately after seeding the cells, then for another 2-hour period 24 hours after seeding the cells.

attachment and flattening of cells on PDL.<sup>49</sup> However, the long-term dynamics of the cellular signal was flat in the plasmonic resonance window, and even somewhat decreased in the proteins and lipids windows. On the other hand, FBS coating resulted in a slower increase in cellular signal for the first hour, but eventually the cellular signal from FBS coating reached a level just below fibronectin coating. This result suggests that surface coatings can differently affect the initial anchoring of cells and their subsequent spreading.

The cellular signal from protein, plasmonic resonance, and lipids windows had similar trend overall, but there were some differences that distinguish between the different spectral windows. For example, there was a clear decrease in the protein and lipids signal for the PDL coating after 1 hour, whereas the plasmonic resonance signal remained somewhat constant. A

possible explanation for this difference is the difference in IR absorption between the surface coatings and cellular matters. For example, the decrease in protein signal for PDL coating may represent its decomposition by the cells. Note that the cellular signal curves in Fig. 4 (b), (d), (f) were calculated by applying PCA to  $\Delta A(\omega, t)$  for each well. By its definition,  $\Delta A(\omega, t = 0) = 0$ , so the corresponding signals clearly show the spectral changes resulting from cellular adhesion, but not the initial contribution from different surface coatings. Instead, Fig. S3 presents the cellular signal with the zero-point set to the mean IR signal for uncoated metasurfaces. Here, different absorbance contribution of each surface coating can be seen clearly. In particular, it becomes clear that PDL has a large contribution to the signal in all three spectral windows, comparable to the signal from fully adhered cells with fibronectin coating. This

could be the consequence of either its higher density or larger thickness, or a combination of the two. In this case, even though the initial rise in signal is most likely attributed to the cells, the subsequent plateau in plasmonic resonance signal and decrease in protein signal may originate from the combined contributions of decreased PDL coating and increased cellular adhesion.

#### IR spectroscopic measurement of protease-activated receptor (PAR) signaling

Next, we demonstrate the measurement of cellular response to compounds that activate cellular signaling in a dose-dependent manner, by using the protease-activated receptor (PAR) signaling pathway as a model. PARs are a family of transmembrane G-protein couple receptors (GPCRs), which are activated by the cleavage of their amino-terminal extracellular domain at a specific site by proteases such as thrombin and trypsin.<sup>50</sup> This unmasks a specific amino acid sequence that acts as a tethered ligand that binds to the receptor to effect transmembrane signaling. Alternatively, synthetic peptides that mimic the tethered ligand domains can also directly activate the receptor, and these peptides have been widely used in the studies of PAR pathways.

Out of the four members of PARs, A431 cells endogenously express PAR1 and PAR2. Stimulating PAR pathways in A431 cells leads to many cellular events downstream, including cytoskeletal reorganization and redistribution of cellular matters. Such dynamic mass redistribution (DMR) of cells in response to the activation of cellular signaling pathway has been previously studied using resonant waveguide grating (RWG) based optical biosensors.<sup>51,52</sup> In particular, A431 cell's response to PAR agonists have been previously studied,<sup>52</sup> demonstrating that there is a positive DMR that starts immediately upon the introduction of PAR agonist, followed by a negative DMR that lasts up to approximately 1 hour. The positive DMR has been attributed to the recruitment of intracellular targets to the activated receptors at the cellular membrane, whereas the negative DMR was attributed to receptor internalization.<sup>51</sup>

In this work, we induce PAR signaling response in A431 cells using PAR activating peptides and observe the cellular response with MEIRS using the multiwell-integrated metasurface. A431 cells were seeded on fibronectin-coated metasurface and cultured in DMEM in a standard cell incubator until confluency. Prior to measurement, the culture medium was replaced with L15 medium for measurement in ambient atmospheric conditions. For the measurement of PAR signaling, we expect the cellular response to last for about 1 hour, thus the 16 min per acquisition for each well used for the previous adhesion measurement does not have enough time resolution to accurately monitor this process. To overcome this issue, instead of cycling between all 16 wells in the structure, we cycled between four wells only, and measure each well every four minutes. Each set of four wells was monitored for one hour. After the measurement of the first set of four wells was complete, another set of four wells was monitored. See Fig. S1(b) for the stage movement pattern. Currently, we need about 1 minute of acquisition time for each spectrum to have

adequate signal-to-noise ratio. Since in our current setup different wells are probed one-by-one sequentially, there is a trade-off between the number of wells measured and the time resolution for each well.

We stimulated the cells with three different PAR peptides: SFLLR-NH<sub>2</sub> for PAR1 activation, SLIGKV-NH<sub>2</sub> for PAR2 activation, and VKGILS-NH<sub>2</sub>, which is a reversed amino acid sequence for SLIGKV, as a control peptide that does not trigger any PAR signaling. Cells were initially kept in L15 medium without any peptides and one spectrum was obtained prior to adding the peptides. Then, PAR peptides in L15 medium were added at different concentrations while the IR spectra were continuously acquired at  $\Delta t = 4$  min time resolution for each well. The results of the PAR activation measurements were analyzed using PCA similarly to the cell adhesion/spreading measurements and are presented in Figure 5.

The IR spectral features associated with PAR response (Fig. 5 (a), (d), (g)) are very similar to that seen from cellular adhesion. However, the temporal change in cellular signals (Fig. 5 (b), (e), (h)) is fundamentally different. For PAR1 activating SFLLR and PAR2 activating SLIGKV peptides, there was rapid increase in the cellular signal as soon as the peptides were added. The cellular signal peaked at about 8-12 minutes after the addition of the peptides, followed by a gradual decrease in cellular signal back to baseline level, which lasted for about 30 min. The cellular signal peak for SLIGKV lasted for 8-12 minutes whereas for SFLLR, the cellular signal decreased right after the maximal point was reached, suggesting different rates of protein trafficking and receptor internalization for PAR1 and PAR2 pathways. At 100  $\mu$ M concentration, the peak amplitudes of cellular signals were similar for SFLLR and SLIGKV. Such temporal cellular signal from PAR activating peptides agree with previous observations based on RWG sensors,<sup>52</sup> as well as our previous observation of cellular response to trypsin through MEIRS.<sup>37</sup> On the other hand, the control peptide VKGILS, which does not trigger PAR signaling, showed very little response from the cells. Note that there was a slight decrease in cellular signal when the peptides were added, and this was particularly visible in the plasmonic resonance window. A possible explanation for this decrease is the perturbation in the temperature or refractive index of the medium caused by the addition of the peptide, to which the plasmonic resonance shift is expected to be more sensitive to, compared to proteins and lipids IR absorption.

In addition to observing different PAR peptides, we have also measured the dose response of A431 cells to SLIGKV by varying the peptide concentration (Fig. 5 (c), (f), (i)). To quantify the dose-dependent response from the temporal cellular signal, the maximum of cellular signal from  $t = 8$  min to  $t = 16$  min (*i.e.* the peak amplitude of the PAR2 response) were plotted. Our result clearly shows that the MEIRS cellular signal in response to SLIGKV is dose dependent and saturable at high concentrations. The experimental data points were fitted with the standard Hill model to obtain the half maximal effective concentration ( $EC_{50}$ ) values. We obtain  $EC_{50} = 7.1 \pm 3.0 \mu$ M,  $7.0 \pm 1.6 \mu$ M, and  $12.4 \pm 8.2 \mu$ M from proteins, plasmonic resonance, and lipids windows, respectively. The  $EC_{50}$  value obtained from proteins

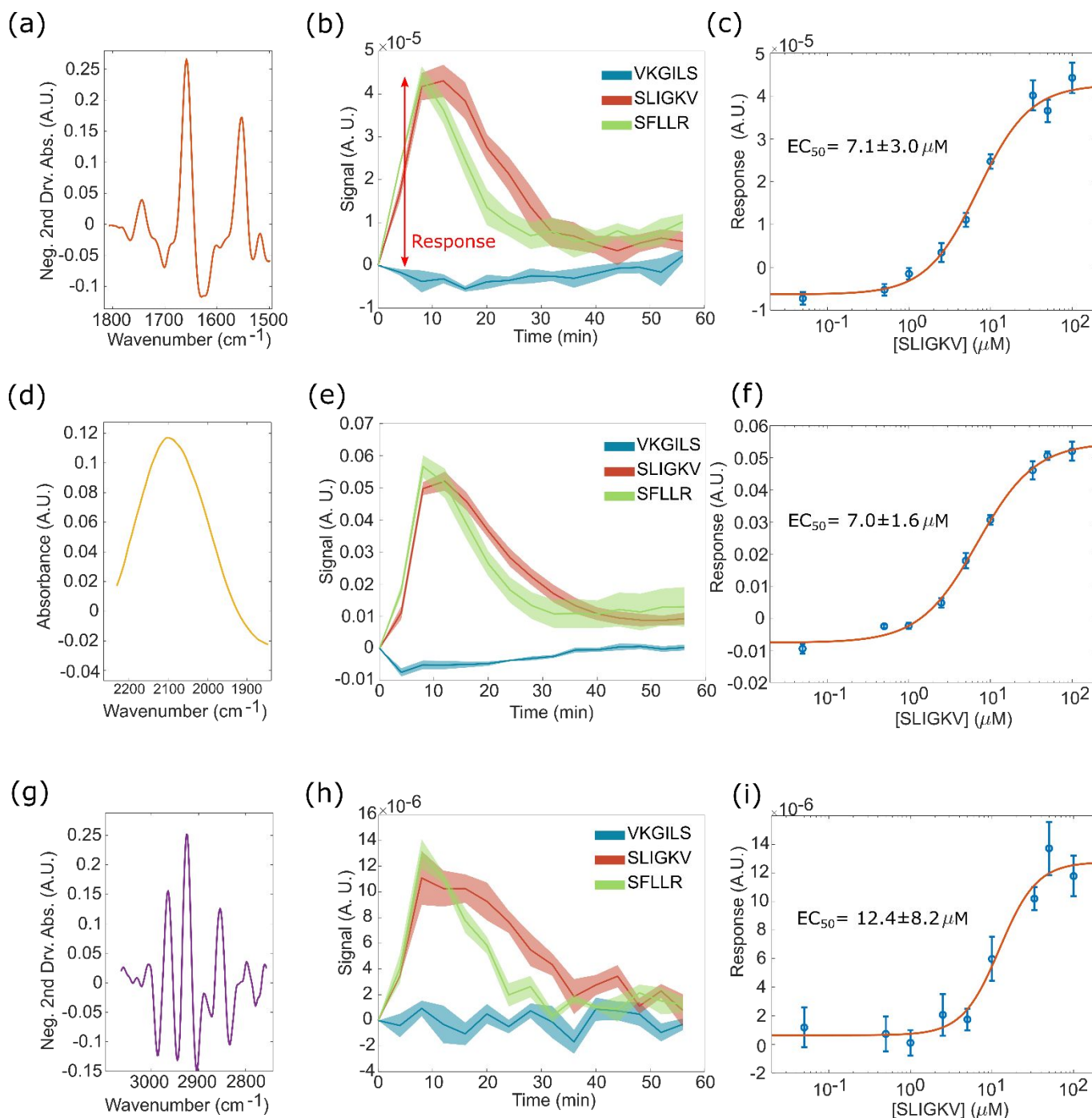


**Figure 5** MEIRS measurement of cellular response to the activation of PAR1/PAR2 receptors by three synthetic peptides. (a), (d), (g): PC1 loading in the protein (a), plasmonic resonance (d), and lipid (g) spectral window. The sign of the 2<sup>nd</sup> derivative absorbance spectra for proteins and lipids have been reversed for more intuitive presentation. (b), (e), (h): Time evolution of protein (b), plasmonic resonance (e), and lipids (h) signal. The amplitude of the peak at approximately 10 min is used to determine the dose response. The solid curves represent the mean, and the shaded areas represents the standard error ( $n = 4$ ). (c), (f), (i): Response of cells to SLIGKV-NH<sub>2</sub> at different doses, measured in the protein (c), plasmonic resonance (f), and lipids (i) windows. Red curve: best fit curve to the Hill model.

and plasmonic resonance window agree well with previous result from RWG sensors ( $EC_{50} = 6.1 \pm 1.0 \mu\text{M}$  from positive DMR).<sup>52</sup> The  $EC_{50}$  value obtained from lipids window is slightly larger and has a much higher uncertainty, but this is likely due to the higher noise in the lipids window, leading to less accurate determination of  $EC_{50}$ .

Lastly, comparing the dominant spectral features from the cell adhesion/spreading experiment (Figs. 4 (a), (c), (e)) and the

PAR activation/signaling experiment (Fig. 5 (a), (d), (g)), we note that the spectral features (*i.e.* the PC1 spectral loadings) extracted from these two experiments were almost identical in each spectral window. This is somewhat surprising because in one case, the spectral features result from change in cell adhesion, and in the other case the spectral change can be attributed to the recruitment of proteins and receptor internalization to/from cellular membrane. Such similarity may

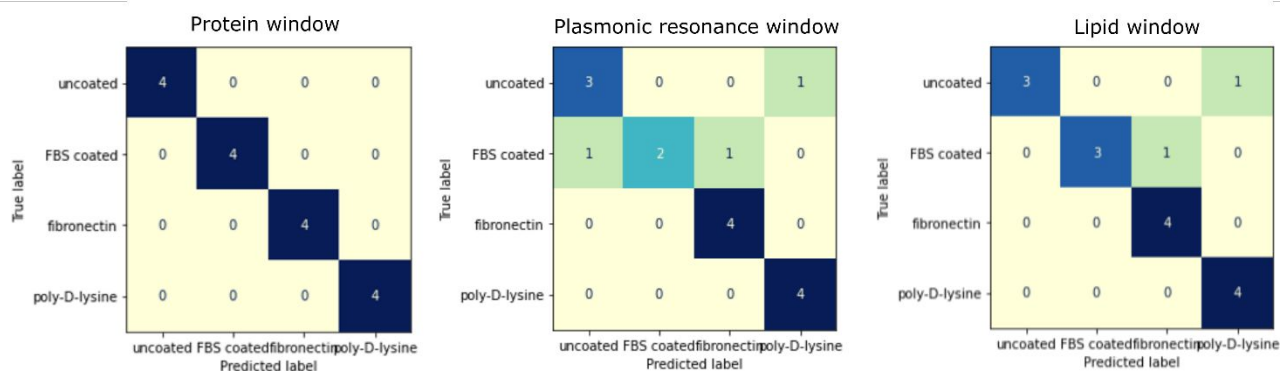


Figure 6. Confusion matrices obtained after subselection of spectral windows for the validation set using PCA-LSTM model.

imply that the cellular matter within the detection zone (*i.e.* metasurface nearfield which penetrates approximately 100 nm into the surrounding) are spectrally highly uniform. Another factor to consider regarding this similarity is that we have focused only on PC1 in our analysis, and thus ignoring small differences in the IR spectra in favor of simplifying quantification of the overall cellular signal. Any small spectral differences that differentiate between different cellular responses may be “buried” in the higher principal components. Also, the spectral change associated with PAR signaling at 100  $\mu$ M peptide concentration is roughly 5 times smaller than that from cellular adhesion. Any small spectral differences that differentiate it from cellular adhesion may be masked by the noise in the measurement. Therefore, improving the signal-to-noise ratio would be an important step in identifying unique spectral features related to cellular processes, and will be the subject of our future work.

#### Deep learning for classification of spectral data generated by cell adhesion to metasurfaces coated with different surface coatings

So far, we have analyzed the IR spectra through the dominant principal component in each spectral region to simplify interpretation. However, the IR spectra collected over time change in a complex manner, and machine learning methods such as deep learning models can play a crucial role in analyzing such spectra. Here, we apply PCA followed by a long-short term memory (LSTM) network to the data collected for the cell adhesion experiment as a proof-of-concept demonstration. The PCA-LSTM model is used to classify the 4 surface coatings from the cellular response.

A detailed description of the PCA-LSTM model is included in the supplementary information. The classification model is built on the training set and then applied to the validation set in a stratified four-fold cross-validation in a total number of 4 replicates for each of the 4 surface coatings. The performance of the developed model is evaluated by the correct classification rate. A confusion matrix is used to evaluate the quality of the output of the classifier for validation set. In the matrix, the elements on the diagonal are the observations that are correctly classified, while the non-diagonal are the ones that are misclassified. Overall, the classification model performance shown in Fig. 6, resulting from the PCA-LSTM model, provided 100% correct classification when cross-validated in the protein

window, 81.25% in the PR window, and 87.5 % correct classification in the lipids window. The high accuracy of the classification model in the protein window suggests that the protein window displays distinguishable spectral features relevant to cell adhesion dynamics and thus the model performance is better. The lower classification accuracy in the lipid window may be related to the low signal-to-noise ratio in the spectral data. In the plasmonic resonance window, we have noticed that there are small differences in the shape of the plasmonic resonance peak across different absorbance spectra, which appear in the 2<sup>nd</sup> principal component; this may have led to the low accuracy in the deep learning model. Even though deep learning models with such small number of data points may not be useful in practice, our proof-of-concept demonstration here shows that in principle, such deep learning models can be combined with spectral data obtained from MEIRS for high-throughput analysis of cellular response.

#### Conclusions

In this work, we have introduced, assembled, and characterized a novel live-cell biosensing platform – Multiwell Integrated Metasurface Array (MIMA) – for the application of MEIRS as a label-free phenotypic assay. Plasmonic metasurfaces were fabricated on microscope slide sized  $\text{CaF}_2$  substrate and integrated with the superstructure for a 16-well cell culture chamber. The measurement of such structure was performed using a home-built inverted FTIR-coupled micro-spectrometer. The effectiveness of our device as a cellular assay was demonstrated through the measurement of cellular adhesion and spreading with different ECM surface coatings, as well as monitoring the cellular response to the activation of PAR signaling pathways and characterizing the cell's dose response to PAR activating peptide. Further, we have demonstrated the applicability of PCA-LSTM deep learning model for the analysis of IR spectra from MEIRS.

While moderately sized ( $1'' \times 3''$ ) metasurface arrays were used in this work, the initial size of the substrate can be increased, and even larger areas can be covered by the metasurface patterns. This would enable metasurface integration with full-sized microplate structures. However, currently we use e-beam lithography to define the metasurface patterns, which can be costly for large area metasurface arrays.

An alternative approach of wafer-scale photolithography has been recently demonstrated for the fabrication of biosensing plasmonic metasurfaces.<sup>50</sup> This approach is highly promising for the mass-production of metasurface-based biosensors, including MIMA devices described here.

The fabrication of metasurface on a planar substrate and integration of such device with standard multiwell structures for cell culture make our device compatible with typical cell culture workflow and handling. The CaF<sub>2</sub> substrate is transparent in the visible band, so our device is compatible with any conventional fluorescence-based techniques as well. Although in this work cells were kept in L15 medium and room temperature, our device is compatible with commercially available stage top incubators for temperature and CO<sub>2</sub> control, which would enable spectroscopic cell characterization under physiological conditions.

The current throughput of our measurement is limited by the acquisition time needed for obtaining a single spectrum at each well, as well as the fact that different wells are measured sequentially. Although we have demonstrated real-time monitoring of live cells for a 16-well device, expanding the device to 96 or 384 well plate would require several hours to probe all the wells and such time resolution may not be acceptable for many applications. One way to increase the acquisition rate is to use linear array or 2D focal plane array detectors to collect the spectrum from multiple wells at the same time.<sup>27,51</sup> Alternatively, the recent progress in tunable QCL systems have attracted much attention to their use in infrared spectroscopy for biological samples.<sup>5,10–12,52</sup> By limiting the sampled wavenumbers to a few selected wavenumbers of interest, such systems can collect the IR spectra and perform chemical imaging with very high acquisition speed. In combination with the MIMA device, such QCL-based system would allow for the monitoring of drug-cell interaction as well as dynamic cellular response to different stimuli with high throughput.

## Experimental Section

### Metasurface Fabrication

The Fano resonant plasmonic metasurface used in this work was fabricated on 4" diameter and 1 mm thick CaF<sub>2</sub> substrates (Toptec Optics Inc., Fuzhou, China). A "flat" cut was made to the CaF<sub>2</sub> to simulate wafer flats, so that the CaF<sub>2</sub> window fit on typical instruments designed for Si wafers. 20 nm of SiO<sub>2</sub> was deposited on the CaF<sub>2</sub> using plasma-enhanced chemical vapor deposition (PECVD) as a protection layer, as we have found that bare CaF<sub>2</sub> slowly dissolves in water, eventually lifting off the metasurface pattern. Polymethyl methacrylate (PMMA) was spin-coated on the CaF<sub>2</sub> substrate as a e-beam resist, followed by another layer of DisCharge to reduce charge buildup. The metasurface pattern was written by electron beam lithography using JEOL 9500 system. The exposed resist was developed using 1:3 MIBK:IPA developer. Gold was then deposited using electron beam evaporation of 5 nm of chromium as adhesion layer followed by 70 nm of gold, and the PMMA resist were

removed through lift-off by soaking the sample in acetone overnight. As the final step, the metasurface sample was coated with 200 nm thick PMMA protective layer and diced to 1" × 3" size using a dicing saw. PMMA was removed again using acetone, and the superstructure for multiwell cell culture chamber (Grace Bio-Labs CultureWell™) was attached to the 1" × 3" metasurface slide.

### Cell culture

Human epidermoid carcinoma cell line A431 (acquired from ATCC, passage number <15) was used as a model system for all measurement. A431 cells were cultured in Dulbecco's modified Eagle medium (DMEM) supplemented by GlutaMAX (Gibco), 10% fetal bovine serum (FBS; Gibco), and 1% penicillin/streptomycin (Gibco) in a standard cell incubator with 5% CO<sub>2</sub> and 37 °C.

Prior to seeding the cells on multiwell integrated metasurface, the metasurface device was first rinsed in 70% ethanol for sterilization and dried in sterile environment. 100 μL of surface coating solutions were added to each well and placed in a cell incubator overnight. The surface coating solutions used in this work included phosphate-buffered saline (PBS, no coating; Gibco), 10% FBS in DMEM (to simulate typical cell culture condition), 10 μg/mL fibronectin (Corning) in PBS, as well as 50 μg/mL poly-D-lysine (PDL; Gibco) in PBS.

For the measurement of cell adhesion on different surface coatings, A431 cells were trypsinized from culture flask and resuspended in Leibovitz's L-15 medium (Gibco) supplemented by 1% antibiotic-antimycotic (amphotericin B, penicillin, streptomycin; Gibco) at approximately 500,000 cells per mL. 200 μL of this cell suspension was added to each metasurface well to seed the cells just prior to measurement.

For the measurement of PAR signalling, the multiwell metasurface device was coated with fibronectin as previously described. A431 cells were trypsinized from cell culture flask and resuspended in DMEM + 10% FBS at approximately 500,000 cells per mL. 200 μL of this cell suspension was added to each metasurface well to seed the cells, and the cells were incubated in a cell incubator overnight. Prior to measurement, the culture medium in each well was replaced by 100 μL of L15 supplemented by 1% antibiotic-antimycotic. Synthetic peptides including SFLLR-NH<sub>2</sub> (Sigma-Aldrich), SLIGKV-NH<sub>2</sub> (Sigma-Aldrich), and VKGILS-NH<sub>2</sub> (Tocris), in 100 μL of L15 at appropriate concentrations were manually pipetted to individual wells to activate PAR signaling.

### FTIR spectroscopy

The multiwell integrated metasurface devices were measured using an in-house external optics add-on to an FTIR spectrometer (Bruker Vertex v70). FTIR measurement was performed at room temperature in ambient air conditions. IR beam from FTIR source is focused on the metasurface pixel using a reflective Cassegrain objective (15X, NA=0.58, Thermo Scientific), resulting in a spot size of approximately 330 μm, slightly larger than the metasurface pixels. However, since the CaF<sub>2</sub>/water interface reflects very little, most of the reflected signal originates from the metasurface. Unpolarized light was used for all measurements.

FTIR spectra were collected at 1 acquisition/minute, 100 averaging for both background and sample, at 4 cm<sup>-1</sup> spectral resolution. Mertz phase correction and 3-term Blackman-Harris apodization function were used.

As post-processing, atmospheric compensation was performed using Bruker OPUS software to subtract water vapor and CO<sub>2</sub> peaks from the collected spectra. The spectral data were then analysed using an in-house MATLAB code. The metasurface reflectance spectra, taken with a patch of gold on CaF<sub>2</sub> as the background, were normalized based on maximum metasurface reflectance and converted to absorbance spectra according to  $A = -\log_{10}(R^{cell}/R^{bare})$ , where  $A$  is the absorbance,  $R^{cell}$  is the reflectance spectra with cells and  $R^{bare}$  is the reflectance spectra of the bare metasurface without cells. The absorbance spectra were further smoothed and differentiated using 21-point Savitzky-Golay filter. For each metasurface, we calculate the absorption difference spectrum as  $\Delta A \equiv A(\omega, t) - A(\omega, t = 0)$ , where  $A(\omega, t = 0)$  is the absorbance spectrum at  $t = 0$ , with (for PAR peptide experiment) or without (for adhesion experiment) cells. Thus, effectively the spectrum at  $t = 0$  was treated as the background spectrum, and we focused on the changes in absorbance spectra from this initial state.

Principal component analysis (PCA) was performed on the processed spectra to obtain the cellular response signals. To simplify the interpretation, three spectral windows were chosen based on the dominant vibrational mode: proteins (1499 cm<sup>-1</sup>–1807 cm<sup>-1</sup>), plasmonic resonance (1845 cm<sup>-1</sup>–2231 cm<sup>-1</sup>), and lipids (2756 cm<sup>-1</sup>–3064 cm<sup>-1</sup>). PCA was performed separately for each spectral window and only the first principal component in each spectral window was considered for interpretation of the cellular signal. PCA was performed separately for cell adhesion data and PAR signalling data, but otherwise all data from each of the two experiments (all four surface coatings, all the peptides and different concentrations) were included in the PCA.

## Author Contributions

SHH and G. Shvets conceived and designed the experiment. SHH and G. Sartorello built the optical setup. SHH and PTS fabricated the metasurface and performed the experiment. SHH and G. Shvets analyzed and interpreted the data. CX developed the deep learning classification model. G. Shvets and OE supervised the project. The manuscript was written through contributions from all authors.

## Conflicts of interest

OE is supported by Janssen, J&J, Astra-Zeneca, Volastra and Eli Lilly research grants. OE is scientific advisor and equity holder in Freenome, Owkin, Volastra Therapeutics and One Three Biotech and a paid scientific advisor to Champions Oncology.

## Acknowledgements

The research reported here was supported by the National Cancer Institute of the National Institutes of Health under award number R21 CA251052 and by the National Institute of General Medical Sciences of the National Institutes of Health under award number R21 GM138947. OE is supported by UL1TR002384, UG3CA244697, R01CA194547, P01CA214274 grants from the National Institutes of Health and LLS SCOR grants 180078-02, 7021-20, 180078-01. This work was performed in part at the Cornell NanoScale Facility, a member of the National Nanotechnology Coordinated Infrastructure (NNCI), which is supported by the National Science Foundation (Grant NNCI-1542081). The authors thank Dr. Ye Fang (Corning Inc.) for insightful discussions on the experimental design using PAR peptides.

## References

- 1 M. J. Baker, J. Trevisan, P. Bassan, R. Bhargava, H. J. Butler, K. M. Dorling, P. R. Fielden, S. W. Fogarty, N. J. Fullwood, K. A. Heys, C. Hughes, P. Lasch, P. L. Martin-Hirsch, B. Obinaju, G. D. Sockalingum, J. Sulé-Suso, R. J. Strong, M. J. Walsh, B. R. Wood, P. Gardner and F. L. Martin, *Nat. Protoc.*, 2014, **9**, 1771–1791.
- 2 F. L. Martin, J. G. Kelly, V. Llabjani, P. L. Martin-Hirsch, I. I. Patel, J. J. Trevisan, N. J. Fullwood and M. J. Walsh, *Nat. Protoc.*, 2010, **5**, 1748–1760.
- 3 E. Goormaghtigh and J. de Meutter, *Anal. Chem.*, 2021, **93**, 3733–3741.
- 4 S. Delbeck and H. M. Heise, *Anal. Bioanal. Chem.*, 2020, **412**, 4647–4658.
- 5 C. K. Akhgar, J. Ebner, O. Spadiut, A. Schwaighofer and B. Lendl, *Anal. Chem.*, 2022, **94**, 5583–5590.
- 6 C. Lacombe, V. Untereiner, C. Gobinet, M. Zater, G. D. Sockalingum and R. Garnotel, *Analyst*, 2015, **140**, 2280–2286.
- 7 D. K. R. Medipally, T. N. Q. Nguyen, J. Bryant, V. Untereiner, G. D. Sockalingum, D. Cullen, E. Noone, S. Bradshaw, M. Finn, M. Dunne, A. M. Shannon, J. Armstrong, F. M. Lyng and A. D. Meade, *Cancers (Basel)*, 2019, **11**, 1–18.
- 8 H. J. Butler, P. M. Brennan, J. M. Cameron, D. Finlayson, M. G. Hegarty, M. D. Jenkinson, D. S. Palmer, B. R. Smith and M. J. Baker, *Nat. Commun.*, 2019, **10**, 1–9.
- 9 M. Lotfollahi, S. Berisha, D. Daeinejad and D. Mayerich, *Appl. Spectrosc.*, 2019, **73**, 556–564.
- 10 M. Schnell, S. Mittal, K. Falahkheirkhah, A. Mittal, K. Yeh, S. Kenkel, A. Kajdacsy-Balla, P. S. Carney and R. Bhargava, *Proc. Natl. Acad. Sci. U. S. A.*, 2020, **117**, 3388–3396.
- 11 K. Yeh, S. Kenkel, J. N. Liu and R. Bhargava, *Anal. Chem.*, 2015, **87**, 485–493.
- 12 S. Mittal, K. Yeh, L. Suzanne Leslie, S. Kenkel, A. Kajdacsy-Balla, R. Bhargava, L. S. Leslie, S. Kenkel, A. Kajdacsy-Balla and R. Bhargava, *Proc. Natl. Acad. Sci.*, 2018, **115**, E5651–E5660.
- 13 L. Chen, H. Y. N. Holman, Z. Hao, H. A. Bechtel, M. C. Martin, C. Wu and S. Chu, *Anal. Chem.*, 2012, **84**, 4118–4125.
- 14 A. Derenne, R. Gasper and E. Goormaghtigh, *Analyst*, 2011, **136**, 1134.
- 15 J. Phelan, A. Altharawi and K. L. A. Chan, *Talanta*, 2020, **211**, 120737.
- 16 A. Altharawi, K. M. Rahman and K. L. A. Chan, *Analyst*, 2019, **144**, 2725–2735.

- 17 D. R. Whelan, K. R. Bambery, L. Puskar, D. McNaughton and B. R. Wood, *Analyst*, 2013, **138**, 3891–3899.
- 18 K. L. A. Chan, S. G. Kazarian, K. L. Andrew Chan and S. G. Kazarian, *Chem. Soc. Rev.*, 2016, **45**, 1850–1864.
- 19 G. Birarda, A. Ravasio, M. Suryana, S. Maniam, H. Y. N. Holman and G. Greci, *Lab Chip*, 2016, **16**, 1644–1651.
- 20 E. Mitri, G. Birarda, L. Vaccari, S. Kenig, M. Tormen and G. Greci, *Lab Chip*, 2014, **14**, 210–218.
- 21 K. L. A. A. Chan, P. L. V. Fale, A. Atharawi, K. Wehbe and G. Cinque, *Anal. Bioanal. Chem.*, 2018, **410**, 6477–6487.
- 22 K. Loutharback, L. Chen and H. Y. N. Holman, *Anal. Chem.*, 2015, **87**, 4601–4606.
- 23 H. Y. N. Holman, R. Miles, Z. Hao, E. Wozel, L. M. Anderson and H. Yang, *Anal. Chem.*, 2009, **81**, 8564–8570.
- 24 K. Loutharback, G. Birarda, L. Chen and H.-Y. N. Holman, *Protein Pept. Lett.*, 2016, **23**, 273–282.
- 25 C. G. Mariangela, Y. Seydou, S. Diego, C. Sabine, M. Augusto and C. Petibois, *Biotechnol. Adv.*, 2013, **31**, 402–407.
- 26 M. K. Kuimova, K. L. A. Chan and S. G. Kazarian, *Appl. Spectrosc.*, 2009, **63**, 164–171.
- 27 C. W. Scott and M. F. Peters, *Drug Discov. Today*, 2010, **15**, 704–716.
- 28 Y. Fang, *Assay Drug Dev. Technol.*, 2006, **4**, 583–595.
- 29 D. Kho, C. MacDonald, R. Johnson, C. P. Unsworth, S. J. O’Carroll, E. du Mez, C. E. Angel and E. S. Graham, *Biosensors*, 2015, **5**, 199–222.
- 30 G. Quaranta, G. Basset, O. J. F. Martin and B. Gallinet, *Laser Photonics Rev.*, 2018, **12**, 1–31.
- 31 B. T. Cunningham, P. Li, S. Schulz, B. Lin, C. Baird, J. Gerstenmaier, C. Genick, F. Wang, E. Fine and L. Laing, *J. Biomol. Screen.*, 2004, **9**, 481–490.
- 32 J. M. Atienza, J. Zhu, X. Wang, X. Xu and Y. Abassi, *J. Biomol. Screen.*, 2005, **10**, 795–805.
- 33 F. A. Atienzar, K. Tilmant, H. H. Gerets, G. Toussaint, S. Speeckaert, E. Hanon, O. Depelchin and S. Dhalluin, *J. Biomol. Screen.*, 2011, **16**, 575–587.
- 34 M. S. Liberio, M. C. Sadowski, C. Soekmadji, R. A. Davis and C. C. Nelson, *PLoS One*, 2014, **9**, e112122.
- 35 K. L. A. Chan, A. S. Shalygin, O. N. Martyanov, T. Welton and S. G. Kazarian, *J. Mol. Liq.*, 2021, **337**, 116412.
- 36 S. G. Kazarian, *Anal. Bioanal. Chem.*, 2007, **388**, 529–532.
- 37 S. H. Huang, J. Li, Z. Fan, R. Delgado and G. Shvets, *Lab Chip*, 2021, **21**, 3991–4004.
- 38 R. Adato and H. Altug, *Nat. Commun.*, 2013, **4**, 2154.
- 39 D. Rodrigo, A. Tittl, N. Ait-Bouziad, A. John-Herpin, O. Limaj, C. Kelly, D. Yoo, N. J. Wittenberg, S.-H. Oh, H. A. Lashuel and H. Altug, *Nat. Commun.*, 2018, **9**, 2160.
- 40 O. Limaj, D. Etezadi, N. J. Wittenberg, D. Rodrigo, D. Yoo, S. H. Oh and H. Altug, *Nano Lett.*, 2016, **16**, 1502–1508.
- 41 C. Wu, A. B. Khanikaev, R. Adato, N. Arju, A. A. Yanik, H. Altug and G. Shvets, *Nat. Mater.*, 2011, **11**, 69–75.
- 42 F. Neubrech, C. Huck, K. Weber, A. Pucci and H. Giessen, *Chem. Rev.*, 2017, **117**, 5110–5145.
- 43 C. Huck, F. Neubrech, J. Vogt, A. Toma, D. Gerbert, J. Katzmann, T. Härtling and A. Pucci, *ACS Nano*, 2014, **8**, 4908–4914.
- 44 P. T. Shen, S. H. Huang, Z. Huang, J. J. Wilson and G. Shvets, *Cells*, 2022, **11**, 1600.
- 45 G. Kelp, N. Arju, A. Lee, E. Esquivel, R. Delgado, Y. Yu, S. Dutta-Gupta, K. Sokolov and G. Shvets, *Analyst*, 2019, **144**, 1115–1127.
- 46 G. Kelp, J. Li, J. Lu, N. Dinapoli, R. Delgado, C. Liu, D. Fan, S. Dutta-Gupta and G. Shvets, *Lab Chip*, 2020, **20**, 2136–2153.
- 47 S. Cai, C. Wu, W. Yang, W. Liang, H. Yu and L. Liu, *Nanotechnol. Rev.*, 2020, **9**, 971–989.
- 48 J. Hutterer, G. Proll, P. Fechner and G. Gauglitz, *Anal. Bioanal. Chem.*, 2022, **414**, 575–585.
- 49 D. Mazia, G. Schatten and W. Sale, *J. Cell Biol.*, 1975, **66**, 198–200.
- 50 S. R. Coughlin, *Nature*, 2000, **407**, 258–264.
- 51 Y. Fang, A. M. Ferrie, N. H. Fontaine, J. Mauro and J. Balakrishnan, *Biophys. J.*, 2006, **91**, 1925–1940.
- 52 Y. Fang and A. M. Ferrie, *BMC Cell Biol.*, 2007, **8**, 1–12.
- 53 A. Leitis, M. L. Tseng, A. John-Herpin, Y. S. Kivshar and H. Altug, *Adv. Mater.*, 2021, **33**, 2102232.
- 54 J. De Meutter, K.-M. Derfoufi and E. Goormaghtigh, *Biomed. Spectrosc. Imaging*, 2016, **5**, 145–154.
- 55 L. Shi, X. Liu, L. Shi, H. T. Stinson, J. Rowlette, L. J. Kahl, C. R. Evans, C. Zheng, L. E. P. Dietrich and W. Min, *Nat. Methods*, 2020, **17**, 844–851.